The Disk Population in a Distant Massive Protocluster

The Astrophysical Journal, 940:124 (17pp), 2022 December 1 https://doi.org/10.3847/1538-4357/ac9b54

The Disk Population in a Distant Massive Protocluster

Yu Cheng[1], Jonathan C. Tan[2,3], John J. Tobin[4], Rubén Fedriani[2], Morten Andersen[5], and Junfeng Wang[6]
[1] National Astronomical Observatory of Japan, 2-21-1 Osawa, Mitaka, Tokyo, 181-8588, Japan; ycheng.astro@gmail.com
[2] Dept. of Space, Earth & Environment, Chalmers University of Technology, SE-412 93 Gothenburg, Sweden
[3] Dept. of Astronomy, University of Virginia, Charlottesville, VA 22904, USA
[4] National Radio Astronomy Observatory, 520 Edgemont Rd, Charlottesville, VA 22903, USA
[5] European Southern Observatory, Karl Schwarzschild Str. 2, D-85748, Garching, Germany
[6] Department of Astronomy, Xiamen University, Xiamen, Fujian 361005, People's Republic of China
Received 2022 July 26; revised 2022 October 17; accepted 2022 October 17; published 2022 November 29

Abstract

The unprecedented angular resolution and sensitivity of the Atacama Large Millimeter/submillimeter Array make it possible to unveil disk populations in distant (>2 kpc), embedded young cluster environments. We have conducted an observation toward the central region of the massive protocluster G286.21+0.16 at 1.3 mm. With a spatial resolution of 23 mas and a sensitivity of 15 μJy beam^{-1}, we detect a total of 38 protostellar disks. These disks have dust masses ranging from about 53 to 1825 $M_{\oplus}$, assuming a dust temperature of 20 K. This sample is not closely associated with previously identified dense cores, as would be expected for disks around Class 0 protostars. Thus, we expect our sample, being flux-limited, to be mainly composed of Class I/flat-spectrum source disks, since these are typically more massive than Class II disks. Furthermore, we find that the distributions of disk masses and radii are statistically indistinguishable from those of the Class I/flat-spectrum objects in the Orion molecular cloud, indicating that similar processes are operating in G286.21+0.16 to regulate disk formation and evolution. The cluster center appears to host a massive protostellar system composed of three sources within 1200 au, including a potential binary with 600 au projected separation. Relative to this center, there is no evidence for widespread mass segregation in the disk population. We do find a tentative trend of increasing disk radius versus distance from the cluster center, which may point to the influence of dynamical interactions being stronger in the central regions.

Unified Astronomy Thesaurus concepts: Protostars (1302); Young stellar objects (1834); Circumstellar disks (235); Protoclusters (1297)

1. Introduction

Circumstellar disks of dust and gas are a common feature of young and forming stellar systems, from deeply embedded Class 0 protostars to more evolved Class II phase or pre-main-sequence stars, at which point the natal envelope has dissipated. These disks play important roles in both star and planet formation (e.g., Armitage 2011; Williams & Cieza 2011). Large samples of disks with high-fidelity imaging obtained by interferometers, such as the Atacama Large Millimeter/submillimeter Array (ALMA), have greatly boosted the study of their formation and evolution. In particular, high-resolution observations in the millimeter continuum allow for constraints on the masses and sizes of dust disks. Surveys of Class II disks to date span a range of physical conditions and ages, e.g., low-mass star-forming regions such as Lupus (1–3 Myr, Ansdell et al. 2016), Taurus (1–3 Myr, Tripathi et al. 2017), and Chamaeleon I (2–3 Myr, Pascucci et al. 2016), and more clustered environments, such as the Orion Nebula Cluster (ONC, <1 Myr, Eisner et al. 2018; Otter et al. 2021), Orion A (1–3 Myr, van Terwisga et al. 2022), σ Orionis (3–5 Myr, Ansdell et al. 2017), and the Upper Scorpius OB association (5–10 Myr, Barenfeld et al. 2016).

Meanwhile, the ensemble properties of dust disks in the protostellar phase (Class 0, Class I, and flat-spectrum) are also being established. In the VANDAM Orion survey toward a sample of 328 protostars, Tobin et al. (2020) found that masses and radii decreased during the protostellar phase. Still, these protostellar dust disks have masses that are systematically larger than those of Class II disks. Surveys of young disks in Perseus reveal a similar mass distribution of Class I disks to Orion, but more massive Class 0 disks (Tychoniec et al. 2020). A systematically less massive and smaller disk population is reported for Ophiuchus (Cieza et al. 2019; Encalada et al. 2021), but this could result from misidentification of disk class rather than being a real difference (Tobin et al. 2020). These observed properties of disks throughout the protostellar phase inform us of both the conditions of their formation and the initial conditions for disk evolution. It is during the protostellar phase that the largest mass reservoir is available for the formation of companions or planets.

Still, further surveys of more diverse samples, especially of massive protoclusters, are necessary to unveil the protostellar disk properties of environments in which most Galactic star formation occurs, and to explore how they might be affected by external environmental factors (e.g., Eisner et al. 2018). However, the above studies are all limited to relatively nearby regions ($d \lesssim 0.5$ kpc). For more distant regions, a complete identification and classification of disks and associated host stars is generally unavailable due to limited spatial resolution and sensitivity for infrared facilities, such as Spitzer Space Telescope and Herschel Space Observatory. Recently, Busquet et al. (2019) showed that it is possible to characterize the disk population in a relatively distant massive protocluster, GGD 27 (~1.4 kpc), with the long-baseline capability of ALMA. In a single pointing they detected 25 compact continuum sources with a resolution of 40 mas (~56 au) and a sensitivity of

millimeter flux equivalent to a gas mass of $\sim$0.002 $M_\odot$ (or a dust mass of $\sim$7 $M_\oplus$ assuming a gas-to-dust ratio of 100).

Here we present an ALMA long-baseline survey of protostellar disks in the central region of a more distant massive protocluster. Our target G286.21+0.17 (hereafter G286) is a massive, gas-dominated protocluster associated with the η Car giant molecular cloud at a distance of 2.5 ± 0.3 kpc (Barnes et al. 2010). This distance is also consistent with the recent estimation based on Gaia DR2 parallax measurements (Zucker et al. 2020). The gas and dust components in the wider region covering the whole protocluster have been previously studied with relatively low-resolution ALMA observations, which revealed $\sim$80 dense cores in millimeter continuum emission and molecular line emission (Cheng et al. 2018, 2020b). In addition, near-IR (NIR) observations with the Very Large Telescope found that a high fraction of the young stellar objects (YSOs) have disks, further suggesting the cluster is very young ($\sim$1 Myr; Andersen et al. 2017). Follow-up multi-epoch Hubble Space Telescope (HST) observations showed that these YSOs with disk excesses also exhibit a higher variability fraction, and some high-amplitude variables are likely associated with accretion outburst events (Cheng et al. 2020a). Here we present high-resolution ALMA observations of the central region of G286, which enable detection and study of the disk population. The paper is organized as follows: a description of the observations is given in Section 2; the results are presented in Section 3; a discussion is made in Section 4; and a summary is given in Section 5.

2. Observations

2.1. ALMA Long-baseline Observations

G286 was observed with ALMA (Project ID 2017.1.01552.S, PI: Y. Cheng) in a single pointing centered on J2000 R.A. = 10:38:32.2, decl. = −58:19:8.5, i.e., the position of the most luminous dense core in this region (Cheng et al. 2018). We employed the C36-10 configuration to achieve the highest spatial resolution in band 6. Five executions were conducted during a period from 2017 October to November, with 44–49 antennas and covering baselines from 40 m to 16,000 m. The precipitable water vapor during observations ranged from 0.4 to 1.2 mm.

The correlator was configured with the first baseband split into two 234.38 MHz spectral windows with 1920 channels each (0.37 km s^{-1} velocity resolution) and centered on H30α and CO(2–1), respectively. The second baseband was set to low-spectral-resolution continuum mode, 1.875 GHz bandwidth divided into 128 31.25 MHz channels, centered at 234.0 GHz. The third baseband was split into three 58.6 MHz spectral windows centered on $C^{18}O$ (2–1), $H_2CO(3_{2,1}–2_{2,0})$, and CH_3OH $(4_{2,2}–3_{1,2})$, respectively. Each spectral window has 960 channels, corresponding to 0.19 km s^{-1} velocity resolution. The fourth baseband was configured with two 234.38 MHz spectral windows (1920 channels, 0.39 km s^{-1} velocity resolution) centered on SiO(5–4) and $SO_2(22_{2,20}–22_{1,21})$. This paper will focus on the continuum results, while the line results will be presented in a future work.

The raw data were calibrated with the ALMA data reduction pipeline using CASA 5.1.1 (McMullin et al. 2007). The continuum visibility data were constructed with all line-free channels. In order to increase the signal-to-noise ratio of the continuum, we performed two rounds of phase-only self-calibration, with the first round using a solution interval that encompassed the length of an entire on-source scan, and the second round using a 6.05 s solution interval, which corresponds to a single integration. We created maps with a Briggs weighting scheme with a robust parameter of 0.5, which yields a resolution of 26 mas × 20 mas, i.e., 65 au × 50 au, with a position angle (PA) of 9°.3. The resultant rms noise in the 1.3 mm continuum was $\sim$15 μJy beam^{-1}. The maximum recoverable scale was $\sim$0.″22, corresponding to 550 au, so our observations are mainly sensitive to very compact structures. The half-power beamwidth is 25″ at observed frequency. The flux accuracy from absolute amplitude calibration is expected to be $\lesssim$10%.

The fiducial image, i.e., made with robust = 0.5, achieves a good compromise between sensitivity and spatial resolution. To test the robustness of observational results, we also created continuum images with natural and uniform weighting, respectively. For the natural weighting, we obtained a synthesized beam of 31 mas × 25 mas and an rms noise of 15 μJy beam^{-1}. For the uniform weighting, we obtained an image with a resolution of 20 mas × 14 mas and an rms noise of 34 μJy beam^{-1}.

2.2. Auxiliary Data

To provide constraints on the larger-scale mass reservoir of detected disks, we make use of the ALMA 1.3 mm continuum map presented in Cheng et al. (2018). These data probe structures with sizes up to 18.″6 (0.23 pc) with a spatial resolution of 1.″07 × 1.″02 (2600 au). The 1σ noise level in this image is 0.45 mJy beam^{-1}. This low-resolution millimeter map mainly traces the thermal dust emission from dense cores in the cloud. We refer to this map as the "1″ resolution" map to distinguish it from the "high-resolution" map made with the long-baseline observation.

3. Results

In Figure 1(a) we present the high-resolution 1.3 mm continuum detections in the G286 region. The background is the 1″ resolution continuum image at the same wavelength, which illustrates the cloud fragments, i.e., dense cores, at $\sim$0.01 pc scales. The spatial resolution of long-baseline data is improved by a factor of $\sim$50 (or by a factor of 2500 in beam area), so the new observations probe physical structures at dramatically different scales, i.e., from $\sim$50 to $\sim$540 au. As we will show later, the high-resolution continuum is mainly tracing emission from protostellar disks, and the vast majority of detections are very compact or partly resolved pointlike sources. The positions of these detections are marked by red crosses in Figure 1(a). They are distributed mainly to the north and southeast of the central position. We enumerate the sources in order of increasing R.A.

In Figure 1(b) we show the high-resolution image in the central 4.″5 field of view (FOV), i.e., the inner region of the most luminous dense core, G286c1, following the designation in Cheng et al. (2020b). The image reveals a triple system (sources 18, 20, 22) in the center, as well as several other compact sources scattered around at distances of about 1.″5–2.″5 (3500–6200 au) from the center. Despite strong spatial filtering, some extended features are also seen. There are a couple of relatively diffuse condensations, located at $\sim$0.″5 to the south of the triple system. They are detected at >4σ level, but do not contain compact point sources. To the northeast of the triple system (separated by $\sim$1.″5) there is a tentative detection of a curved filamentary feature, which may be related

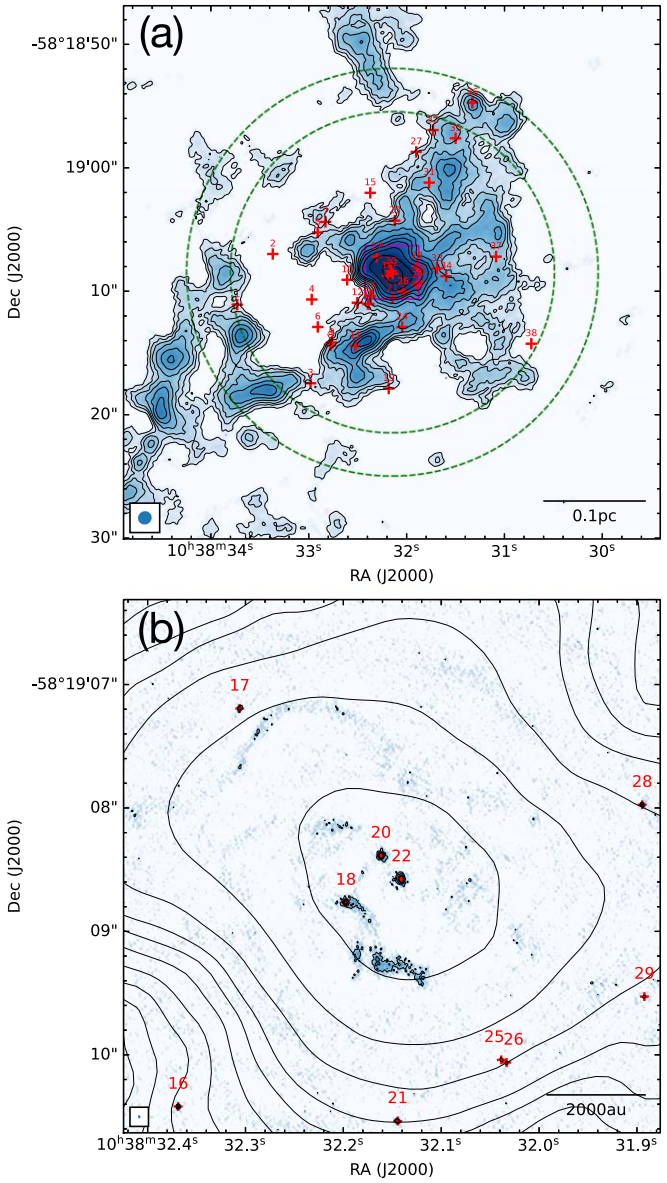

Figure 1. (a) Overview of compact continuum source detections in G286. Their positions are indicated with red crosses. The background is the low-resolution (∼1″, or 2500 au) 1.3 mm continuum image from Cheng et al. (2018), shown in blue colorscale and contours. The contour levels are (4, 6, 8, 11, 15, 20, 25, 30, 40, 60, 100) × 0.45 mJy beam^{-1}. The beam size of the low-resolution data, 1.″12 × 1.″07, is indicated in the bottom left corner. The long-baseline observation is a single pointing centered on J2000 R.A. = 10:38:32.2, decl. = −58:19:8.5, and the inner and outer dashed green circles mark the boundaries where the primary beam correction factor corresponds to 0.5 and 0.3, respectively. The magenta box indicates the region shown in (b). (b) A zoom-in view showing the detections in the central 4.″3 field of view. The blue colorscale and contours illustrate the long-baseline continuum image. The contour levels are (4, 8, 16, 32) × 15 μJy beam^{-1}. The black contours are the same as in (a). The beam size of the long-baseline image, 26 mas × 20 mas, is indicated in the bottom left corner.

to density enhancements shaped by complex gas motions on scales of a few times 0.01 pc. Its morphology is suggestive of an accretion stream to the central protostars.

3.1. Source Identification

We run the *dendrogram* algorithm (Rosolowsky et al. 2008) implemented in *astrodendro* to carry out an automated, systematic search for protostellar disks in the high-resolution continuum image. Here we focus on the identified leaf structures (the base element in the hierarchy of *dendrogram* that has no further substructure). We tested different combinations of parameters, and for the fiducial case we set the base flux density threshold to 5σ, the minimum significance for structures to 1σ, and the minimum area to 0.26 × the synthesized beam. This set of parameters ensures the robustness of detections. The minimum area, i.e., 0.26 $\theta_{\rm beam}$, corresponds to the measured area in *dendrogram* for an isolated 6σ point source (in *dendrogram* the area only accounts for pixels with values above the base level, i.e., 5σ in our case). The search is run on the image before primary beam correction so that the rms noise is relatively uniform. However, the rms in the neighborhood of strong sources can be locally elevated due to imperfect cleaning and dynamic range limitations. In light of this, we first run *dendrogram* with a global rms σ = 15 μJy beam^{-1}, then each detection is examined with the same criteria again with the rms replaced by a local value. The local rms is estimated in an annulus around each source from 0.″1 to 0.″2, which ranges from 15 to 39 μJy beam^{-1} (after primary beam correction). Moreover, since we focus on the protostellar disks in this work, some relatively extended structures have been manually removed. This happens only in the central region shown in Figure 1(b) for the diffuse emission to the south of the triple system.

The identification gives a final catalog of 38 compact sources. In Figure 2 we present close-up images for all the sources. In addition to the triple system in the center, we have also discovered three possible binary systems: sources 8, 9, separated by 620 au, sources 13, 14, separated by ∼150 au, and sources 25, 26, separated by ∼130 au. Since the region is highly clustered, we only consider multiple systems with projected separation $\lesssim$1000 au as candidate multiples. Most detections appear as unresolved or marginally resolved point-like sources, but some strong sources, including sources 10, 18, 20, 22, and 36, are better resolved and some extended low-level emission is also seen. Sources 10 and 36 appear to have larger aspect ratios. We assume these detections are all associated with protostellar disks given their compact sizes ($\lesssim$200 au if located at 2.5 kpc).

To examine the level of possible contaminants from extragalactic sources, we take the deep 1.2 mm ALMA survey of submillimeter galaxies in González-López et al. (2020) as a reference (see also Aravena et al. 2016; Fujimoto et al. 2016; Muñoz Arancibia et al. 2022). In this work the number density of submillimeter galaxies is $19{,}300^{+4700}_{-4400}$ per square degree for a flux density above 0.1 mJy. This would translate into a number of $0.79^{+0.19}_{-0.18}$ in our FOV (inside the FWHM of the primary beam) for >6σ (∼0.1 mJy beam^{-1}) detections. Thus we expect no more than one extragalactic contaminant in our sample.

3.2. Characterization of the Disks

To measure the fluxes and sizes of the disks from their 1.3 mm emission we fit 2D Gaussians using the imfit task in CASA. The results are listed in Table 1. Following Tobin et al. (2020), we adopt the 2σ size of the deconvolved major axis as a proxy for the disk radius. If the intensity distribution is well described by a 2D Gaussian model, the 2σ radius is approximately the radial point that contains 90% of the total flux density in the curve-of-growth methodology employed by Ansdell et al. (2016). Six disks (sources 4, 8, 9, 13, 24, 31) are unresolved and could not have their deconvolved sizes

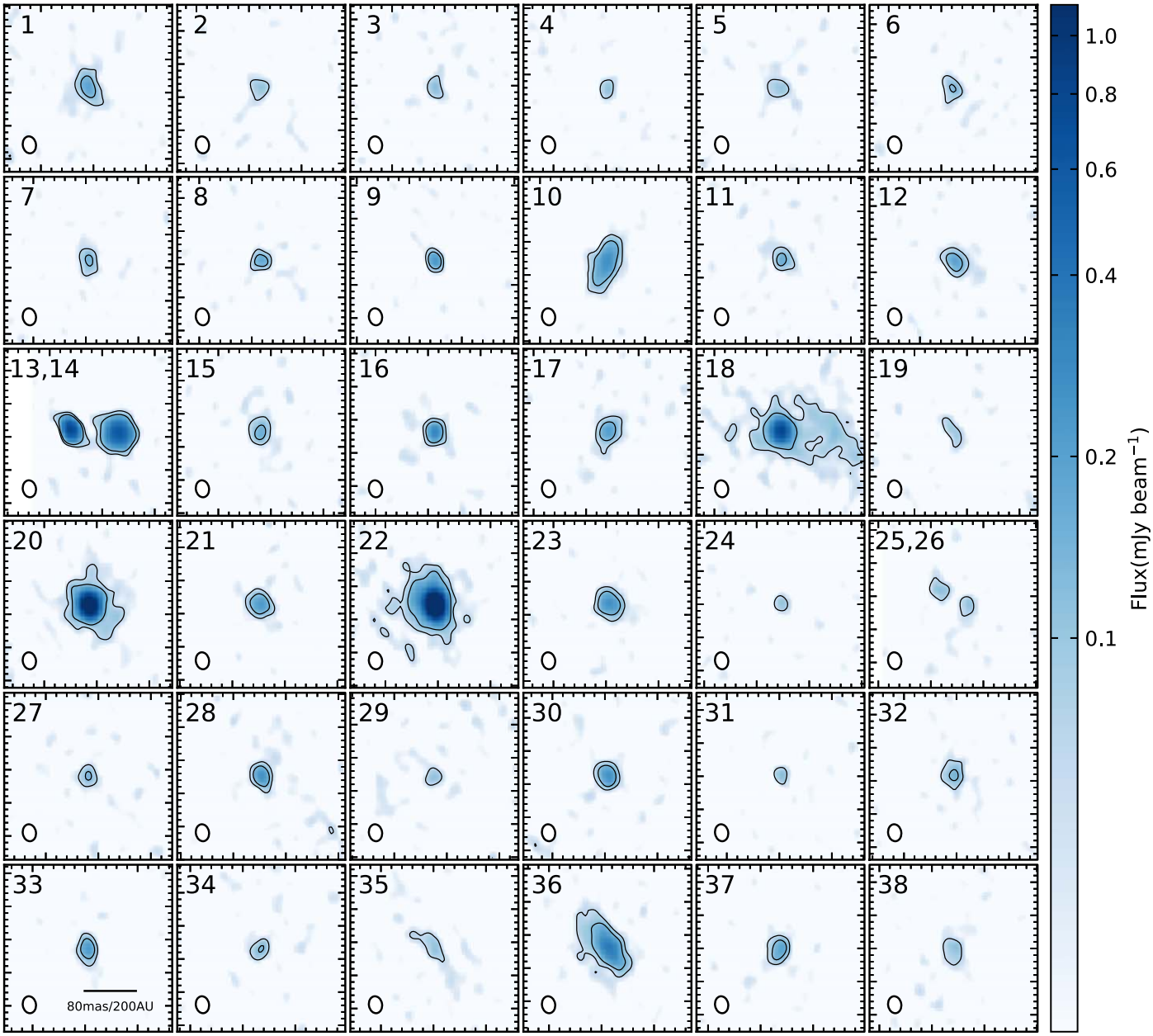

Figure 2. (a) 1.3 mm continuum images of the protostellar disks in G286. The contours levels are (4, 8) × 15 μJy beam^{-1}. The beam size, 26 mas × 20 mas (65 au × 50 au), is shown in the bottom left corner of each panel. The close binary systems (sources 13 and 14; sources 25 and 26) are shown each within a single panel.

constrained in the Gaussian fit. To derive upper size limits for these sources, we run a series of experiments by generating synthetic disk images as a function of disk radius and signal-to-noise ratio (S/N), which are then used as input for a Gaussian fit to determine the minimum deconvolvable radius. We found that this radius is around 40 au for modest S/N of 7–30. The median radius in our sample, with upper limit measurements included, is 55 au. The first and third quartiles of the radius distribution are 43 and 67 au, respectively. There is a tendency for disks in multiple systems to be smaller, although the sample size is relatively small, i.e., nine disks. These nine disks all have disk radii <62 au, with a median $\lesssim$40 au. This trend is similar to that found in ρ Oph, Taurus and Orion (e.g., Cox et al. 2017; Manara et al. 2019; van Terwisga et al. 2022), suggesting that the formation (and evolution) of close multiple star systems affects the observable disk properties.

We use the flux densities to calculate the mass of the protostellar disks, assuming that the emission is purely optically thin isothermal dust emission, enabling us to use the equation

$$M_{\rm dust} = \frac{d^2 F_\nu}{\kappa_\nu B_\nu(T_{\rm dust})}, \quad (1)$$

where d is the distance to the source, i.e., 2.5 kpc, F_ν is the observed flux density, B_ν is the Planck function, $T_{\rm dust}$ is the dust temperature, and κ_ν is the dust opacity at the observed frequency ν. We adopt $\kappa_{1.3\,\rm mm} = 0.899\,{\rm cm^2\ g^{-1}}$ from Ossenkopf & Henning (1994) (thin ice mantles, $10^6\,{\rm cm^{-3}}$ density). We multiply the calculated dust mass by 100, assuming a dust-to-gas mass ratio of 1:100 (Bohlin et al. 1978), to obtain the gas mass. The average dust temperature we

Table 1
Compact ALMA 1.3 mm Continuum Sources in G286

Label	α(J2000) (hh:mm:ss)	δ(J2000) (dd:mm:ss)	$\mathrm{FWHM_{decon}}$ (mas × mas)	PA (deg)	rms (μJy beam^{-1})	Peak (μJy beam^{-1})	Flux (μJy)	Dust Mass ($M_\oplus$)	Gas Mass ($M_\odot$)	Radius (au)	Dense Cores	HST F110W/F160W	X-Ray
G286d1	10:38:33.7310	−58:19:11.093	41 × 25	26	32	361	977	443	0.133	87	-	-	-
G286d2	10:38:33.3676	−58:19:6.987	27 × 19	−22	20	155	299	135	0.041	57	-	-	Y
G286d3	10:38:32.9820	−58:19:17.454	24 × 13	12	25	196	306	139	0.042	51	-	-	-
G286d4	10:38:32.9697	−58:19:10.671	-	-	18	128	166	75	0.023	<40	-	-	-
G286d5	10:38:32.9091	−58:19:5.241	39 × 24	56	17	126	322	146	0.044	83	-	Y	-
G286d6	10:38:32.9077	−58:19:12.897	27 × 18	14	17	161	301	136	0.041	57	-	-	-
G286d7	10:38:32.8296	−58:19:4.389	32 × 15	7	18	171	319	145	0.043	68	Y	-	-
G286d8	10:38:32.7782	−58:19:14.394	-	-	19	214	286	130	0.039	<40	-	-	-
G286d9	10:38:32.7652	−58:19:14.163	-	-	18	288	290	131	0.039	<40	-	-	-
G286d10	10:38:32.6072	−58:19:9.078	57 × 22	−24	16	279	1012	459	0.138	121	-	-	-
G286d11	10:38:32.5234	−58:19:14.424	34 × 17	56	17	189	362	164	0.049	72	Y	-	-
G286d12	10:38:32.5036	−58:19:10.932	31 × 19	52	15	194	411	186	0.056	66	-	-	-
G286d13	10:38:32.3958	−58:19:11.040	-	-	21	811	937	425	0.127	<40	-	Y	-
G286d14	10:38:32.3871	−58:19:11.043	29 × 27	−88	17	631	1593	722	0.217	62	-	Y	-
G286d15	10:38:32.3718	−58:19:2.028	29 × 22	8	18	181	393	178	0.053	62	-	-	-
G286d16	10:38:32.3688	−58:19:10.419	15 × 13	−46	16	310	409	185	0.056	32	-	-	-
G286d17	10:38:32.3059	−58:19:7.194	35 × 20	−34	17	198	445	202	0.061	74	Y	-	-
G286d18	10:38:32.1974	−58:19:8.766	22 × 21	78	24	795	1369	620	0.186	47	Y	-	-
G286d19	10:38:32.1826	−58:19:17.883	48 × 6	31	22	138	311	141	0.042	102	-	-	-
G286d20	10:38:32.1616	−58:19:8.385	14 × 14	56	19	1943	2596	1176	0.353	30	Y	-	-
G286d21	10:38:32.1445	−58:19:10.536	26 × 19	61	15	219	432	196	0.059	55	Y	-	-
G286d22	10:38:32.1407	−58:19:8.577	16 × 12	13	18	3051	4026	1825	0.548	34	Y	-	Y
G286d23	10:38:32.1197	−58:19:4.284	26 × 22	51	16	267	577	261	0.078	55	-	-	-
G286d24	10:38:32.0455	−58:19:12.900	-	-	17	110	117	53	0.016	<40	Y	Y	Y
G286d25	10:38:32.0386	−58:19:10.041	25 × 15	44	15	110	202	91	0.027	53	Y	-	-
G286d26	10:38:32.0333	−58:19:10.062	29 × 17	−10	15	109	189	86	0.026	62	Y	-	-
G286d27	10:38:31.9019	−58:18:58.710	20 × 19	−50	24	205	330	150	0.045	42	-	-	Y
G286d28	10:38:31.8947	−58:19:7.974	20 × 13	27	19	257	370	168	0.050	42	Y	-	-
G286d29	10:38:31.8924	−58:19:9.528	22 × 15	56	17	111	171	77	0.023	47	Y	-	-
G286d30	10:38:31.8695	−58:19:9.288	20 × 17	59	18	260	417	189	0.057	42	Y	-	-
G286d31	10:38:31.7698	−58:19:1.200	-	-	20	151	136	62	0.019	<40	-	-	-
G286d32	10:38:31.7306	−58:18:56.943	30 × 21	1	27	254	564	255	0.077	64	-	-	-
G286d33	10:38:31.6894	−58:19:8.163	25 × 11	4	15	225	347	157	0.047	53	Y	Y	-
G286d34	10:38:31.5965	−58:19:8.784	25 × 14	−56	16	138	231	105	0.031	53	-	-	-
G286d35	10:38:31.4998	−58:18:57.609	60 × 12	39	27	195	569	258	0.077	127	Y	Y	-
G286d36	10:38:31.3289	−58:18:54.720	52 × 25	37	39	983	3432	1555	0.467	110	Y	-	-
G286d37	10:38:31.0862	−58:19:7.200	28 × 16	−27	20	246	477	216	0.065	59	-	-	-
G286d38	10:38:30.7259	−58:19:14.249	41 × 23	10	30	222	583	264	0.079	87	-	-	-

adopt for a protostellar system is assumed to be 20 K. If temperatures of 15 K or 30 K were to be adopted, then the mass estimates would differ by factors of 1.48 and 0.604, respectively. If a higher dust temperature of 100 K is assumed (suitable for typical massive sources, e.g., Zhang et al. 2014), then the mass estimate would decrease by a factor of 0.158. Our measured dust disk masses range from 53 to 1825 $M_\oplus$, with a median of 172 $M_\oplus$. The first and third quartiles of the mass distribution are 136 and 261 $M_\oplus$, respectively. The corresponding total (gas) masses are from 0.016 to 0.55 $M_\odot$ with a median of 0.052 $M_\odot$.

Note that different weighting schemes adopted in the imaging process could also affect the measured disk fluxes, especially for detections with modest statistical significance (S/N $\lesssim$ 10). For example, in the case of uniform weighting (20 mas × 14 mas resolution), bright disks are better resolved, but we fail to detect most disks, i.e., only eight out of 38 disks still have peaks with S/N > 6. The measured fluxes are systematically smaller, but consistent within 35%. For the natural weighting image (31 mas × 25 mas resolution), the measured fluxes are larger than the fiducial values but mostly consistent within 25%, with a few cases larger by $\lesssim$50%. This is partly due to the fact that the Gaussian fitting is capturing more extended emission in lower-resolution images, as evidenced by similarly larger deconvolved radii.

3.3. Correspondence with NIR and X-Ray Sources

To better characterize the properties of the disks, we check their correspondences with data at other wavelengths, which are listed in Table 1. First we cross-match our sample with NIR data. We use a catalog generated from the HST-WFC3/IR data presented in Cheng et al. (2020a). Source detections are done in the F110W and F160W bands down to a 4σ limit, leading to a final catalog of ∼13,000 members inside a 6′ × 6′ field in G286, which also covers our FOV here (Y. Cheng et al. 2022, in preparation). We found that six disks also exhibit an NIR counterpart within 0.″05 (see Appendix A), i.e., sources 5, 13, 14, 24, 33, and 35, suggesting their association with relatively evolved YSOs or a viewing angle and local extinction conditions that enable escape of NIR light from the protostar. Here 0.″05 roughly corresponds to the separations of close binary systems in the disk sample, and our HST catalog has position accuracy better than 0.″05 even for relatively fainter sources.

We also search for infrared counterparts via a SIMBAD and Vizier coordinate search with a 1″ radius. G286d8 and G286d9 appear to coincide with the infrared source 2MASS J10383269-5819143 (Cutri et al. 2003). And the triple system G286d18/20/22 is associated with the infrared source G286.2086+00.1694 (Mottram et al. 2007) (see also the multiwavelength images in Appendix B). These two infrared sources are resolved into some extended emission and/or are not centered on the disks in the F110W/F160W images (see Appendix A), and hence are not contained in our HST catalog. Given the limited angular resolution in relevant infrared surveys we are unable to explicitly identify the specific disk that corresponds to the infrared source.

We next cross-match our sample with an X-ray source catalog (from a census made with Chandra/ACIS observation (PI: J. Tan), J. Wang et al. 2022, in preparation). Pre-main-sequence (PMS) stars, both with and without disks, are well known to emit X-rays that can penetrate the heavy extinction of molecular clouds (Feigelson et al. 2007), thus X-ray observations, particularly with the subarcsecond resolution with Chandra/ACIS, are highly efficient in selecting PMS stars in stellar clusters. We found four disks (sources 2, 22, 24, 27) that coincide with X-ray sources within 0.″5, with one of them (source 24) also having an NIR counterpart.

3.4. Correspondence with Dense Cores

We also check the correspondence of disks with the dense cores identified in the 1″ resolution 1.3 mm continuum image, which traces the dust on 0.01–0.2 pc scales, thus providing constraints on the surrounding environment of the disks. Class 0/I disks are expected to still reside within dense cores, while more evolved sources are not. Here we define that a disk is associated with a dense core if it is located within the core boundary defined by *dendrogram* in Cheng et al. (2018). This criterion selects 16 disks.

However, 11 of these are associated with G286c1, the massive "core" in the center of the FOV. Among these disks the triple system of sources 18, 20, and 22 appears to contain at least one actively accreting protostar: it is located near the emission peak of G286c1 (see Figure 1), shows some evidence for surrounding diffuse emission features that may be accretion streamers, and appears to be the source of a wide-angle bipolar outflow (Y. Cheng et al. 2022, in preparation). The other eight disks (sources 17, 21, 25, 26, 28, 29, 30, 33) are also likely to still be embedded in dense, dusty gas, but it is unclear whether they are all still actively accreting from this material. An intermediate-resolution observation is needed to search for local concentration of millimeter emission around these sources. Only five disks are associated with cores other than G286c1, i.e., sources 7, 10, 18, 35, and 36.

However, we notice that even disks that still reside in dense cores appear to deviate from the emission peaks of cores, in contrast with the expectation for Class 0 disks. Some of these associations may be coincidental, i.e., due to projection effects. If we use a more stringent criterion for cross-matching between disks and cores, i.e., requiring disks to be located within 0.″5 (1250 au) of emission peaks of dense cores, this will result in only two cases (source 36 and source 18/20/22).

Note that the millimeter fluxes of Class 0 systems are envelope-dominated and should be strong enough to be detected in our 1″ resolution image. To elaborate this we compare the G286 results with an Atacama Compact Array (ACA) 0.87 mm survey of 300 protostars in Orion (Federman et al. 2022), where it is found that over 80% of Class 0 systems have envelope fluxes greater than 200 mJy. This corresponds to a mass limit of 1.1 $M_\odot$, and translates into ∼2 mJy at 1.3 mm at a distance of 2.5 kpc, assuming a temperature of 20 K and a dust mass opacity law of $\kappa = (\nu/100\ \mathrm{GHz})\ (\mathrm{g\ cm^{-2}})$. This is marginally larger than the 4σ level of the 1″ resolution continuum (σ = 0.45 mJy). Thus if we assume the G286 disk population has similar envelope properties to those in Orion, then in the low-resolution map we should be able to detect the associated local peaks from envelopes for most protostars in the Class 0 stage. On the other hand, over 80% of Class I or flat-spectrum systems have envelope fluxes smaller than 200 mJy, or masses lower than 1.1 $M_\odot$ (Federman et al. 2022), thus our 1″ resolution observation is not sensitive enough to capture envelope fluxes from most protostars later than Class 0.

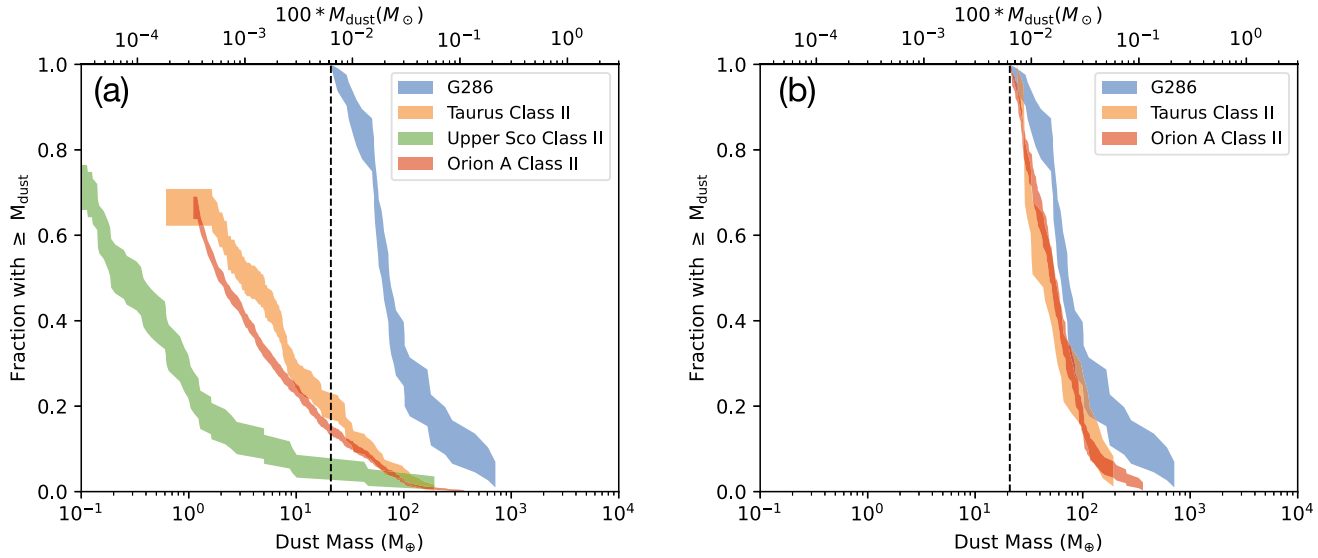

Figure 3. (a) Cumulative distributions of dust disk masses in G286 compared to the Class II disk populations in Taurus (Tripathi et al. 2017), Upper Sco (Barenfeld et al. 2016), and Orion A cloud (van Terwisga et al. 2022). For comparison we recompute the disk masses in G286 using a uniform temperature of 20 K and a dust mass opacity law of $\kappa = (\nu/100\ \mathrm{GHz})^{\beta}$ (g cm^{-2}), where $\beta = 1$. The dashed black line indicates the minimum detectable mass of 21 $M_{\oplus}$ in G286. The plots were constructed using survival analysis and the Kaplan–Meier estimator as implemented in the Python package *lifelines* (Davidson-Pilon et al. 2019). The width of the cumulative distributions plotted represents the 1σ uncertainty of the distribution. (b) Same as (a) but for Taurus and Orion A region we only include disks with dust masses exceeding the minimum detectable mass in G286, i.e., 21 $M_{\oplus}$. The distribution for Upper Sco is not shown as there are only three disks that satisfy this criterion.

Overall, the results suggest that most of our detected disks are Class I or later-stage sources, with only a minority being Class 0. Still for a substantial fraction that do overlap with millimeter continuum emission in the 1″ resolution map, it is difficult to be certain of their evolutionary stage. Intermediate-resolution millimeter continuum observations, as well as observations sensitive to the presence of outflows and dense gas tracers, will help resolve their status.

On the other hand, the detections of circumstellar disks also inform us of the statuses of dense cores, i.e., whether they are starless or protostellar. A related question concerns the absence of detected disks near the centers of many of the dense cores in G286 (see Figure 1). This could be due to these cores being prestellar in nature or having disks that are too faint (low-mass and/or low-temperature) to be detected by the ALMA long-baseline observation. Our 6σ detection sensitivity corresponds to a gas mass of 0.012 $M_{\odot}$ (or a dust mass of 41 $M_{\oplus}$) assuming 20 K temperature. Using the Orion protostellar disk survey in Tobin et al. (2020) as a template, with such sensitivity we can detect ∼50% of disks in their sample (see Section 4.1.2). Therefore, it is likely that some cores in G286 are forming stars with disks undetectable in this survey.

4. Analysis and Discussion

4.1. Comparison with the Disk Population in Nearby Regions

4.1.1. Comparison with Class II Disks

Our long-baseline observation provides a new opportunity to characterize the disk population in a massive protocluster at a distance of 2.5 kpc. The vast majority of the disks are newly detected and we do not have prior knowledge of their classifications. We expect the sample contains mostly protostellar disks prior to Class II stage, since Class II disks are generally fainter and less likely to be detected with our sensitivity. To examine this, in Figure 3 we compare the disk mass distribution of G286 with those of Class II disks in nearby regions. The disk samples in Taurus (Tripathi et al. 2017), Orion A (van Terwisga et al. 2022), and Upper Sco (Barenfeld et al. 2016) are shown as representatives, with the former two being relatively young regions (1–3 Myr), and the latter being an older region (5–10 Myr). In general, Class II dust disks have systematically lower masses with increasing age of the stellar population, and hence the mass distributions of other regions with intermediate ages, such as Lupus and Chamaeleon I, lie in between the selected regions (e.g., Ansdell et al. 2016; Pascucci et al. 2016; Tobin et al. 2020). These Class II disk surveys usually adopt a uniform temperature of 20 K and a dust mass opacity law of $\kappa = (\nu/100\ \mathrm{GHz})^{\beta}$ (g cm^{-2}), where $\beta = 1$. For comparison we recompute the disk masses in G286 with the same assumptions.

The dust disk mass distributions are shown as cumulative distributions using survival analysis implemented in the Python package *lifelines* (Davidson-Pilon et al. 2019). The left-censored fitting functions are used to account for upper limits derived from the nondetections, so the fraction does not reach unity at the low-mass end for Taurus, Orion A, and Upper Sco. For G286 the left-censored data are not available since we do not have prior information on the expected positions of disks from other surveys, so the low-mass part of the cumulative distribution is dominated by the sensitivity limit, but still the high-mass end ($M \gtrsim 100\ M_{\oplus}$) should be relatively well constrained. We find that the disk mass distribution in G286 is systematically higher than those of Class II disks by a factor of $\gtrsim$3.

To account for different sensitivity limits, we also show the cumulative distribution for subsamples of Taurus and Orion A that only include disks with dust masses exceeding the minimum detectable mass in G286, i.e., 21 $M_{\oplus}$ (the distribution for Upper Sco is not shown as there are only three disks that satisfy this criterion). The distinction is less dramatic when the

Table 2
Disk Mass and Radius Sample Comparison

Sample	Mass		Radius	
	Log-rank	KS	Log-rank	KS
G286 vs. Orion (all)	0.088	0.075	0.049	0.17
G286 vs. Orion Class 0	0.0010	0.0022	0.015	0.060
G286 vs. Orion Class I	0.42	0.20	0.25	0.50
G286 vs. Orion Class flat-spectrum	0.58	0.16	0.33	0.71
G286 vs. Taurus Class II	0.013	0.022	···	···
G286 vs. Orion A Class II	0.0072	0.012	···	···

observations are biased toward brighter sources, but the G286 disks are still systematically more massive. To establish the statistical significance of these differences, we use the two-sample log-rank test as implemented in *lifelines* and present the results in Table 2. It is a nonparametric test for censored data sets to characterize the probability (p-value) that the two samples are randomly drawn from the same parent population. The mass distributions of G286 are inconsistent with being drawn from the same distributions as Taurus or Orion A subsamples ($p < 0.05$). The probability values from the Kolmogorov–Smirnov (KS) test are also shown as an additional check on the robustness of the log-rank test.

Thus the G286 sample is less likely to be Class II dominated, but should be mostly composed of protostellar disks. It is possible that the G286 sample contains a fraction of Class II disks. The minimum detectable disk mass in our sample is $\sim 21\ M_\oplus$ (assuming 20 K and $\kappa_{1.3\mathrm{mm}} = 2.3\ \mathrm{g\ cm^{-2}}$). One can see that for Taurus, Orion A, and Upper Sco there exists a small fraction of Class II disks with masses exceeding this limit, i.e., ~20% for Taurus and Orion A and 5% for Upper Sco. Indeed, in Section 3.4 we have found four disks that are associated with X-ray emission, which are likely arising from Class II or Class I YSOs (e.g., Feigelson & Montmerle 1999).

4.1.2. Comparison with Protostellar Disks in Orion

We next compare the disk properties in G286 with those of the protostellar disk sample in the Orion molecular cloud presented in Tobin et al. (2020), which measures the disk properties with the same methodology and using similar wavelength data (0.87 mm) as our study. Again to account for different temperature assumptions in mass estimation, we recompute the disk masses in Orion using a uniform temperature of 20 K. As shown in Figure 4, the Orion disks have slightly larger masses than G286 at the high-mass end ($M \gtrsim 200\ M_\oplus$). The two distributions diverge significantly at the low-mass end due to different sensitivity limits. The radius distributions are broadly similar for disks with $r > 60$ au, which can be better resolved in our observations, but in G286 we have not detected disks with radii greater than 150 au.

To account for the biases induced by different sensitivity and spatial resolution limits, we reprocess the Orion sample to simulate our observational setups in G286 with the following procedures. First, we take the Gaussian component (deconvolved $\mathrm{FWHM_{major}}$ and $\mathrm{FWHM_{minor}}$ axes, integrated flux density in 0.87 mm) of each disk in the Orion sample from Tobin et al. (2020). The major/minor disk axes (in angular units) are then scaled by the distance ratio $d_{\mathrm{Orion}}/d_{\mathrm{G286}} = 0.17$. The flux density is scaled from 0.87 mm to 1.3 mm according to the expectation of thermal dust emission,

$$F_\nu \propto \frac{B_\nu(T_{\mathrm{dust}}) \times \kappa_\nu}{d^2}, \tag{2}$$

where F_ν is the dust emission flux density at frequency ν, $B_\nu(T_{\mathrm{dust}})$ is the Planck function with dust temperature T_{dust}, d is the target distance, κ_ν is the dust opacity, and we assume $\kappa_{0.87\mathrm{mm}} = 1.84\ \mathrm{g\ cm^{-2}}$ and $\kappa_{1.3\mathrm{mm}} = 0.899\ \mathrm{g\ cm^{-2}}$ (Ossenkopf & Henning 1994). The dust temperature has been estimated in Tobin et al. (2020) based on a scaling relation with the bolometric luminosities. Then for each disk we can generate a simulated image by convolving the Gaussian component with our observational beam. Artificial Gaussian noise is also added (before convolution) to ensure that the final image has the same rms level as in our observations, i.e., 15 μJy beam^{-1}. Finally we run the same detection and characterization method described in Sections 3.1 and 3.2 on these simulated images to obtain the reprocessed Orion sample.

In this way we are able to detect ~230 disks in Orion out of a sample of 477 disks, and their distributions in mass and radius are shown in Figure 4. The simulated Orion sample clearly has distributions that are in better agreement with those of G286 after correction for the observational biases. The Orion sample has a larger median mass of $235^{+259}_{-117}\ M_\oplus$ than G286 ($172^{+89}_{-36}\ M_\oplus$), but a similar median radius (57^{+26}_{-15} au versus 55^{+12}_{-12} au). Here the sub- and superscripts on the median values correspond to the first and third quartiles of the distributions. To establish the statistical significance of these differences, we use the two-sample log-rank test as implemented in *lifelines* and the KS test, and the results are presented in Table 2. We find that the mass and radius distributions of G286 are marginally consistent with being drawn from the same distributions as the simulated Orion sample at 90% confidence ($p < 0.1$). From the KS test the radius distributions between two samples are consistent with being drawn from the same distribution ($p = 0.17$).

We further compare the disks of G286 with those in subgroups of the simulated Orion sample with different classifications, i.e., Class 0, Class I, and flat-spectrum. The cumulative distributions and statistical tests are presented in Figure 5 and Table 2, respectively. Interestingly, we find that for both masses and radii, the probability that the two distributions are drawn from the same distribution increases with the evolution stage of the subgroups in Orion, from Class 0 to Class I/flat-spectrum. For the mass distribution the probability that the two distributions are drawn from the same distribution is 1.0×10^{-3} for the Class 0 group, 0.42 for Class I, and 0.58 for the flat-spectrum group. Similarly the radius distribution of G286 is inconsistent with that of the Orion Class 0 sample ($p = 0.015$), but statistically indistinguishable from the Class I and flat-spectrum samples ($p = 0.25, 0.33$).

A natural explanation is that the G286 sample has a low fraction of Class 0 disks and mainly consists of Class I/flat-spectrum disks. This agrees with the results in Section 3.4, where we cross-matched disks with dense cores. Most disks exhibit significant offsets relative to the continuum emission peaks on a 0.01 pc scale, indicating they are not deeply embedded Class 0 objects. In this scenario there is no significant difference in disk properties between G286 and Orion, suggesting similar regulation in disk formation and evolution in the two regions. The fraction of Class 0 disks in

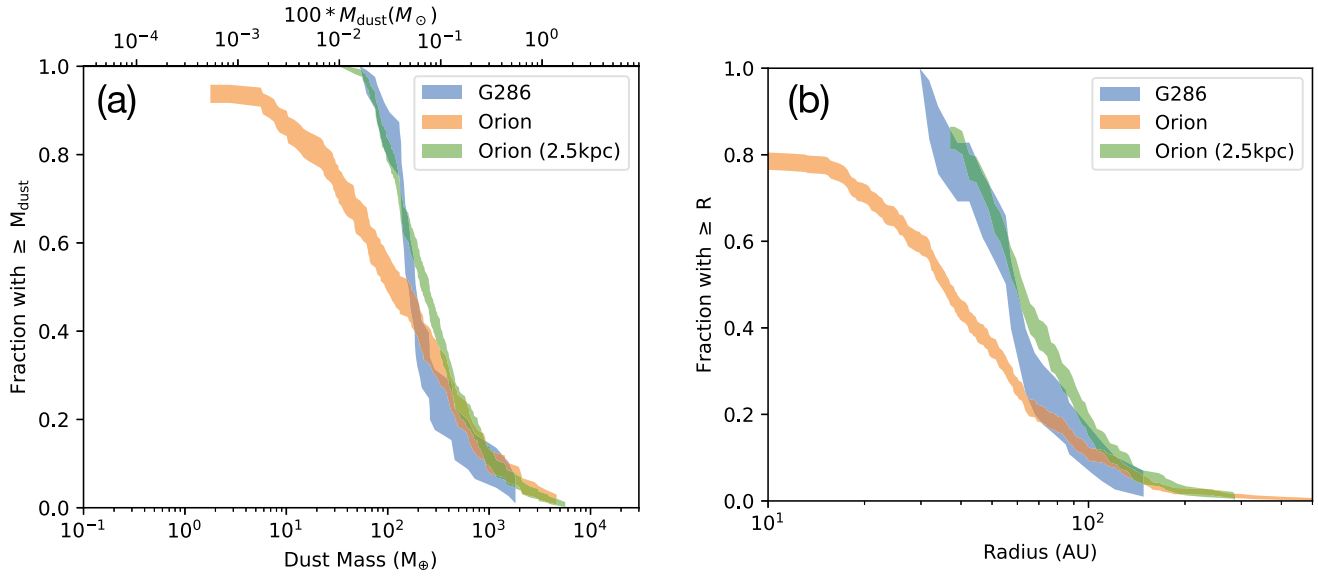

Figure 4. (a) Cumulative distributions of dust disk masses in G286 compared with the Orion sample in Tobin et al. (2020). The mass distribution of the original Orion sample is shown in orange. The reprocessed Orion sample, after correcting for different target distances and observational setups, is shown in green. (b) Same as (a) but for disk radii.

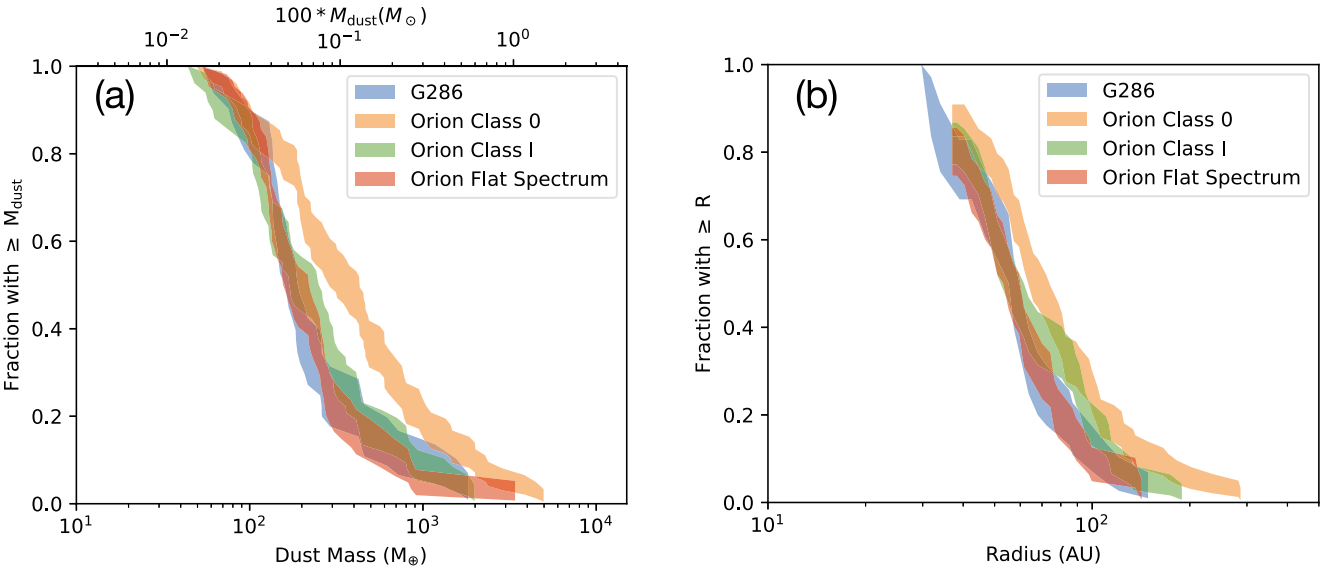

Figure 5. (a) Cumulative distributions of dust disk masses in G286 compared with subgroups of the simulated Orion sample in Tobin et al. (2020) with different classifications. The Class 0 sources in Orion are significantly higher in mass than G286. The Class I and flat-spectrum protostars in Orion are in reasonable agreement with G286. (b) Same as (a) but for disk radii. Similarly the Class 0 sources in Orion are systematically larger than G286 while the Class I and flat-spectrum protostars in Orion are similar to G286.

G286 can be roughly estimated as $4/38 \sim 10\%$, if we classify the four disks that are close to emission peaks of dense cores (i.e., sources 18, 20, 22, 36) as Class 0 stage (or analogous to Class 0 for high-/intermediate-mass YSOs). This is significantly lower than the fraction in Orion, i.e., $94/328 \sim 29\%$ (Tobin et al. 2020).

The G286 protocluster is characterized as being a highly clustered environment, with a high gas mass surface density ($\gtrsim$0.3 g cm^{-2} for the central 15″ FOV, Cheng et al. 2020b), making it different from most regions in Orion and other nearby star formation regions. In spite of different physical conditions, the differences in disk mass/radius distribution between G286 and Orion are potentially explained as being due to a variation in evolutionary status, i.e., relative fraction of Class 0/I/flat-spectrum objects, and there is no indication of a systematic difference in disk properties.

Similarly, Tobin et al. (2020) examined subgroups of disks within Orion that have different environmental conditions, such as L1641 and the Integral-Shaped Filament region, and found no significant variations. Surveys in Perseus also reveal a similar mass distribution of Class I disks to that in Orion, although the Class 0 disks appear to be more massive (Tychoniec et al. 2020). In contrast, the Orion protostars of all classes have systematically higher disk dust masses than those in Ophiuchus (e.g., Cieza et al. 2019; Encalada et al. 2021), but this may be due to a sample classification issue instead of a true difference (see Tobin et al. 2020, for a discussion).

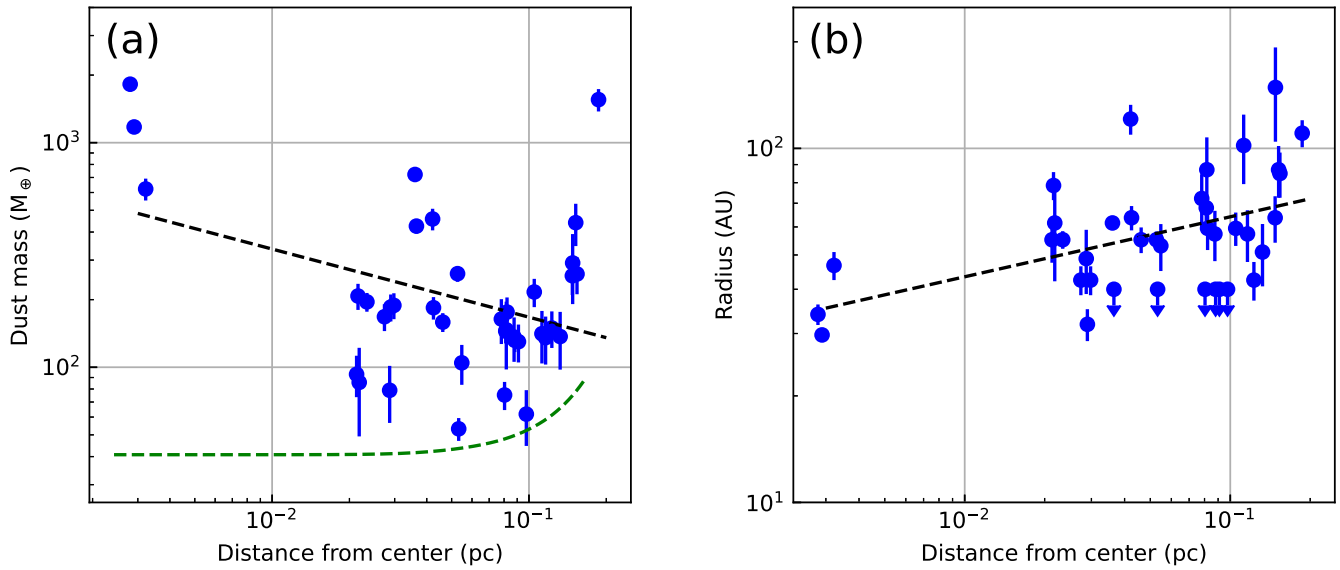

Figure 6. (a) Scatter plot of disk mass against the distance from cluster center (see text for details). The black line shows a linear fit to the data. The green curve indicates the 6σ detection threshold. The rms noise varies with distance from the cluster center, which is also the phase center of the observation, due to beam response. The error bars only account for uncertainties from Gaussian fitting. The typical flux uncertainty from Gaussian fitting is 10%–25%. The estimation of disk mass also relies on assumptions for the temperature and dust properties. (b) Same as (a) but for disk radii. The typical uncertainties for the radius estimation are 10%–20% from the Gaussian fitting.

The similarity in disk dust properties among regions may suggest limited environmental dependence of disk properties. However, one may wonder whether such consistency is universal, especially when some environmental factors that are known to be important in regulating disk formation and evolution, such as strength of magnetic field (e.g., Li et al. 2014), are taken into account. Further surveys covering more environments are needed to shed more light on this issue. Moreover, our analysis here also highlights the importance of uniform observational setups and methodologies when performing comparisons among different regions.

4.2. Disk Properties Relative to the Cluster Center

We check for possible trends between disk properties and the separation from the cluster center. Here the cluster center is defined as the position of dense core G286c1, i.e., the emission peak of the $1''$ resolution 1.3 mm continuum map. This is a reasonable choice from a cluster formation perspective, since G286c1 is located at the central hub where two large-scale filaments intersect (Cheng et al. 2020a). Furthermore, it is the most massive dense core in G286 and hosts a massive multiple system in formation. We have also attempted to define the cluster center in other ways, e.g., using the average position of disks/dense cores, and found that it does not affect the main conclusion of this section.

In Figure 6 we show scatter plots of disk mass and disk radius versus projected distance from the cluster center. There is a lack of disks for distances from 0.004 to 0.02 pc. This is similar to the distribution observed in the GGD 27 cluster, which Busquet et al. (2019) suggests may be caused by disks being impacted by a central massive star(s) or central crowded cluster environment. From Figure 6 there appear to be weak trends for lower disk masses and larger disk radii with increasing projected distance. A linear fit in log–log space gives the following relations:

$$\log(M/M_\oplus) = (-0.30 \pm 0.12)\log(D/\mathrm{pc}) + (1.92 \pm 0.17), \quad (3)$$

and

$$\log(R/\mathrm{au}) = (0.17 \pm 0.05)\log(D/\mathrm{pc}) + (1.98 \pm 0.07). \quad (4)$$

While there is large scatter seen in the figures, the trends appear to have potential significance, i.e., with the indices being $\gtrsim 3\sigma$ from a flat relation.

To further check the strength of the correlations, we use the Spearman rank coefficient test, which assesses how well the relationship between two variables can be described using a monotonic function. The Spearman test returns a value ρ between -1 and $+1$ and an associated p-value to assess the significance of the correlation. A Spearman correlation of 1 results when the two variables being compared are positively related, whereas negative values of ρ represent a negative correlation.

As summarized in Table 3, there is no significant correlation between mass and distance, with $\rho = -0.10$ and $p = 0.554$. This negative correlation becomes stronger and marginally significant ($\rho = -0.30$, $p = 0.081$) if we exclude the three disks with distance greater than 0.15 pc, where the detections are more severely affected by beam response. However, the triple system in the center is associated with more massive YSOs and thus presumably has disk temperatures higher than 20 K, leading to overestimated disk dust masses. If the triple system is excluded, we see no clear trend between mass and distance from Table 3 (and Figure 6).

On the other hand, there is a modest correlation between radius and distance ($\rho = 0.41$–0.55), which seems to be relatively robust ($p = 0.001$–0.026 for different subsamples). This correlation remains for disks that are not contained in multiple systems ($\rho = 0.45$, $p = 0.023$).

Table 3
Statistical Tests for Correlations between the Disk Properties and the Distance from Cluster Center

Sample[a]	Number of Disks	Mass vs. Distance		Radius vs. Distance	
		Spearman ρ	p-value	Spearman ρ	p-value
G286 (all)	38	−0.10	0.554	0.55	0.001
G286 (distance > 0.01 pc)	35	0.13	0.454	0.41	0.026
G286 (distance < 0.15 pc)	35	−0.30	0.081	0.43	0.019
G286 (nonmultiple)	29	0.14	0.477	0.45	0.023

Note.
[a] We consider four samples for the statistical tests: the total 38 disks; 35 disks with the massive triple system in the center removed (i.e., distance > 0.01 pc); 35 disks excluding the three detections where the beam response is smaller than 0.5 (i.e., distance < 0.15 pc); and 29 disks that are not contained in multiple systems (see Section 3.1).

One environmental factor that could result in a radial dependence of disk properties is photoevaporation from massive stars, if these tend to be located at the cluster center. Incident EUV radiation fields are expected to reduce the masses and radii of protoplanetary disks by photoevaporating the gas (e.g., Hollenbach et al. 2000; Nicholson et al. 2019), leading to a decreasing trend in disk masses/sizes with proximity to the ionizing star. Such an effect has been claimed in the ONC (Mann et al. 2014; Eisner et al. 2018), but deeper disk surveys have disputed this result (Otter et al. 2021). While the observed trend of radii in G286 is seemingly in line with the prediction of photoevaporation, we do not expect it to be an effective mechanism, because the ionizing flux is much weaker than in ONC. The stellar mass of G286c1 is not well constrained from its spectral energy distribution (SED) from mid- to far-infrared wavelengths (see Appendix B). If we assume the fluxes are contributed by a dominating component in the triple system, a range of protostellar properties, i.e., a central mass of 4–12 $M_{\odot}$, can yield SEDs that are consistent with the observation. But in any case, G286c1 is still in an early embedded phase and has not developed a large H II region.

Disk truncation by dynamical interactions is another process that could lead to a radial dependence of disk mass and disk size on radial location in the cluster. The trend of disk radii to increase with distance could indicate that strong dynamical interactions in the central region are more common than in the cluster outskirts. Alternatively, the trend may reflect inherited properties of protostellar cores, e.g., if the initial cores tend to be smaller in the higher-pressure central regions, i.e., as expected in the turbulent core model (McKee & Tan 2003), and if disk sizes are related to initial core sizes.

Finally, we note that there are relatively large uncertainties in the deconvolved sizes from Gaussian fits in cases of relatively low S/N (<10), and it is likely that we overestimate the dust disk size when the disk emission becomes confused by background noise, e.g., in the case of source 35. A systematic variation of noise properties with radial position in the cluster could thus also influence these results. A more sensitive and complete survey of the G286 disk population is needed to further explore this tentative trend of disk radii growing with radial position in the cluster.

4.3. Mass Segregation

We further examine whether there is a signature of mass segregation in the disk population, i.e., whether the most massive disks (inferred by millimeter continuum emission) are more centrally concentrated and/or clustered than expected from a random distribution. If there is a correlation between disk mass and protostar mass, then such a mass segregation signal could be due to stellar dynamical mass segregation. Such mass segregation is observed in dynamically old stellar clusters, but also in very young regions, suggesting the segregation is at least partially primordial (e.g., Meylan 2000; Gennaro et al. 2011). Observations of 0.002–0.1 pc scale dense cores, i.e., the progenitors of single stars or small multiple systems, seem to support this argument, since at least a modest level of segregation is found in many molecular clouds (Kirk et al. 2016; Parker 2018; Plunkett et al. 2018; Dib & Henning 2019; Sadaghiani et al. 2020; Nony et al. 2021). However, this is not true for all star-forming regions (e.g., Dib & Henning 2019; Sanhueza et al. 2019). It is still unclear when and how such primordial segregation develops and how its level evolves from dense cores to the YSO stage with the impact of fragmentation and further accretion (Alcock & Parker 2019). If we assume a correlation between the disk mass and stellar mass (e.g., Pascucci et al. 2016), then the current mass segregation level of protostars in G286 can be estimated by examining the spatial distribution of the disk population.

Following Allison et al. (2009), the mass segregation ratio ($\Lambda_{\rm MSR}$) is

$$\Lambda_{\rm MSR} = \frac{L_{\rm norm}}{L_{\rm massive}} \pm \frac{\sigma_{\rm norm}}{L_{\rm massive}}, \quad (5)$$

where $L_{\rm massive}$ is the average path length of the minimum spanning tree (MST) of the N most massive sources, and $L_{\rm norm}$ is the average path length of the MST of N random sources in the cluster. We take the average over 1000 random sets of N sources in the cluster to estimate $L_{\rm norm}$ and its statistical deviation. $\Lambda_{\rm MSR}$ greater than unity indicates a concentration or clustering of massive sources with respect to the random sample. The larger is $\Lambda_{\rm MSR}$, the more mass segregated is the sample.

Figure 7 displays (with orange lines) the mass segregation ratio as a function of number of mass-ranked members ($N_{\rm MST}$). The diagram shows values of $\Lambda_{\rm MSR}$ close to unity, suggesting no mass segregation in the sources as ranked by protostellar disk mass. This is partly due to the existence of source 36, which is located close to the edge of the FOV, but has the second largest mass among the sample, thus driving $L_{\rm massive}$ to a very large value. If we only account for sources with $d < 0.15$ pc, i.e., with source 36 removed, then we have a large $\Lambda_{\rm MSR}$ of 32 for $N_{\rm MST} = 2$, and $\Lambda_{\rm MSR} \gtrsim 3$ for $N_{\rm MST} \leqslant 5$. Therefore, in the inner region, i.e., excluding source 36, there is evidence for mass segregation. One caveat is that the dust disk masses for sources 18, 20, and 22 could be overestimated if the

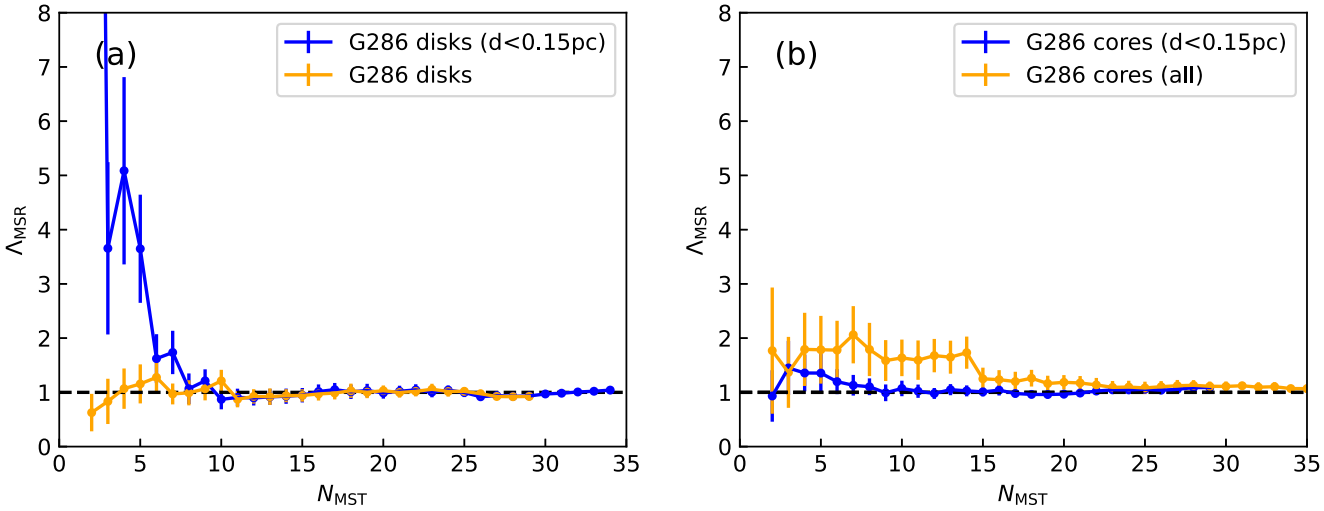

Figure 7. (a) Mass segregation ratio Λ_{MSR} as a function of the N_{MST} most massive disks of G286. The blue line indicates the results when we use only the sources within 0.15 pc from the cluster center, while the orange line indicates the results for all the disks listed in Table 1. (b) Mass segregation ratio Λ_{MSR} for the dense cores in G286. The blue line indicates the results when we use only the sources within 0.15 pc from the cluster center, while the orange line indicates the results for all the disks cataloged in Cheng et al. (2020a).

disk temperatures are much higher than the assumed 20 K, given that they are associated with high-/intermediate-mass star formation (Appendix B).

We have also calculated the Λ_{MSR} parameter for the dense core sample in G286 using the catalog in Cheng et al. (2020a), as shown in Figure 7. We first limit the core sample to have a similar spatial range to the disks, i.e., within 0.15 pc from the cluster center. This gives Λ_{MSR} around 1, suggesting no significant mass segregation. If all the cores in Cheng et al. (2020a) are used, then there appears to be a weak trend of mass segregation, with $\Lambda_{MSR} \sim 1.5$ for $N_{MST} < 15$. Therefore, overall there is no obvious mass segregation of cores in G286.

In summary, for both dense core and disk population in G286, there is no strong evidence for widespread mass segregation, but high-mass star formation, as evidenced by the example of G286c1 and its associated protostellar sources, is located at the cluster center. Our disk sample is mainly composed of Class I/flat-spectrum objects that have been decoupled from their parental cores. Assuming the current observed dense core sample has similar properties to the cores that host these disks, the observation indicates that there is no significant variation in the mass segregation level from cores to protostars.

We also note that the scaling relation between disk dust mass and stellar mass is mainly established for Class II disks (e.g., Ansdell et al. 2016, 2017; Pascucci et al. 2016), which may originate from a mixture of both the initial conditions and the evolutionary process (Manara et al. 2022). It is less clear whether such correlation still holds for protostellar disks. Qualitatively, disk masses do tend to be greater for more massive protostellar systems in the large-scale hydrodynamics disk population synthesis (Bate 2018). A tighter correlation is expected in simulations that render gravitationally self-regulated protostellar disks that are in a marginally gravitationally unstable state (Xu & Kunz 2021; Xu 2022). However, from the observational side this correlation has been less studied. Considering the large dispersion in this relation even for Class II disks (∼0.6–0.9 dex in disk dust mass values for a given stellar mass, see Manara et al. 2022), the segregation in disk dust mass may not robustly reflect that of the protostar population. Nevertheless, the properties of this segregation are an observable that can be compared to simulations that aim to predict disk properties in protocluster environments.

Another limiting factor here is that our disk detections are limited to a relatively small FOV, i.e., within ∼0.15 pc from the center, and the rms noise is higher with larger distance from center due to beam response, thus hindering detection of low-mass disks at the cluster outskirts. Again, a more complete and deeper disk survey would help to explore the question of mass segregation more fully.

5. Conclusions

We have utilized the long-baseline capability of ALMA to conduct a survey of protostellar disks in the massive protocluster G286.21+0.16 at a distance of 2.5 kpc. With a resolution of 23 mas (58 au) and a sensitivity of 15 μJy beam^{-1} (0.002 $M_\odot$, assuming 20 K), we detected 38 compact continuum sources in the 1.3 mm continuum, most of which should be tracing protostellar disks. These disks have dust masses ranging from 53 to 1825 $M_\oplus$ assuming a temperature of 20 K. The median dust disk mass and radius are 172 $M_\oplus$ and 52 au, respectively. Among the sample there is a triple system located at the center of the cluster, as well as three binary systems.

We have suggested that this sample is mainly composed of Class I/flat-spectrum disks, since they are typically not closely associated with dense cores as expected for disks in Class 0 stage, while Class II sources would generally be too faint to be detected. Also, we have found that there is no statistical difference in the distributions of disk masses and radii between the G286 sample and the Class I/flat-spectrum objects in the Orion molecular cloud, indicating that disk formation and evolution in these different regions undergoes similar regulation.

We have found a tentative trend of increasing disk radius with projected distance from the cluster center.

Photoevaporation is not expected to be the cause of such a trend, leaving dynamical interactions or inherited properties from natal cores as possible explanations. We did not find strong evidence for mass segregation in either the disk or dense core population. However, if we restrict to the inner 0.15 pc, then there is some evidence for mass segregation in the disk population. In any case, the most massive core and its associated massive disk systems are located in the center of the cluster. The detailed properties of this massive protostellar system will be explored in more detail in a follow-up paper, including analysis of the line emission from this ALMA observation.

This work demonstrates the capability to characterize the disk populations in embedded protoclusters at distances as great as 2.5 kpc with ALMA at 1.3 mm. If shorter wavelengths, e.g., 0.9 mm, are used, then similar spatial resolutions (∼50 au) can be achieved for targets at ∼4 kpc. More distant regions could also be feasible if spatial resolution is not particularly important. This allows for characterization of protostellar disks, as well as multiplicity, in regions that span a wide range of physical conditions. The presented work can potentially serve as a template for surveys of larger samples to study the environmental dependence of disk properties.

J.C.T. acknowledges support from NSF grant AST-2009674 and ERC Advanced Grant 788829 (MSTAR). R.F. acknowledges funding from the European Union's Horizon 2020 research and innovation program under the Marie Sklodowska-Curie grant agreement No. 101032092. J.W. acknowledges support by the National Science Foundation of China (NSFC) grant 12033004. Y.C. thanks Tie Liu and Xing Lu for initiating a generous invitation to the Shanghai Astronomical Observatory (SHAO) in Shanghai, China, where much of this paper was written. This paper makes use of the following ALMA data: ADS/JAO.ALMA#2017.1.00552.S. ALMA is a partnership of ESO (representing its member states), NSF (USA) and NINS (Japan), together with NRC (Canada), MOST and ASIAA (Taiwan), and KASI (Republic of Korea), in cooperation with the Republic of Chile. The Joint ALMA Observatory is operated by ESO, AUI/NRAO and NAOJ. The National Radio Astronomy Observatory is a facility of the National Science Foundation operated under cooperative agreement by Associated Universities, Inc.

Facilities: Atacama Large Millimeter/submillimeter Array (ALMA), Hubble Space Telescope (HST).

Software: CASA (McMullin et al. 2007), APLpy (Robitaille & Bressert 2012), Astropy (Astropy Collaboration et al. 2013).

Appendix A
Disk Counterparts at NIR Wavelength

In Figures A1 and A2 we present the HST F160W map of G286, and zoom-in views for disks with NIR counterparts, respectively.

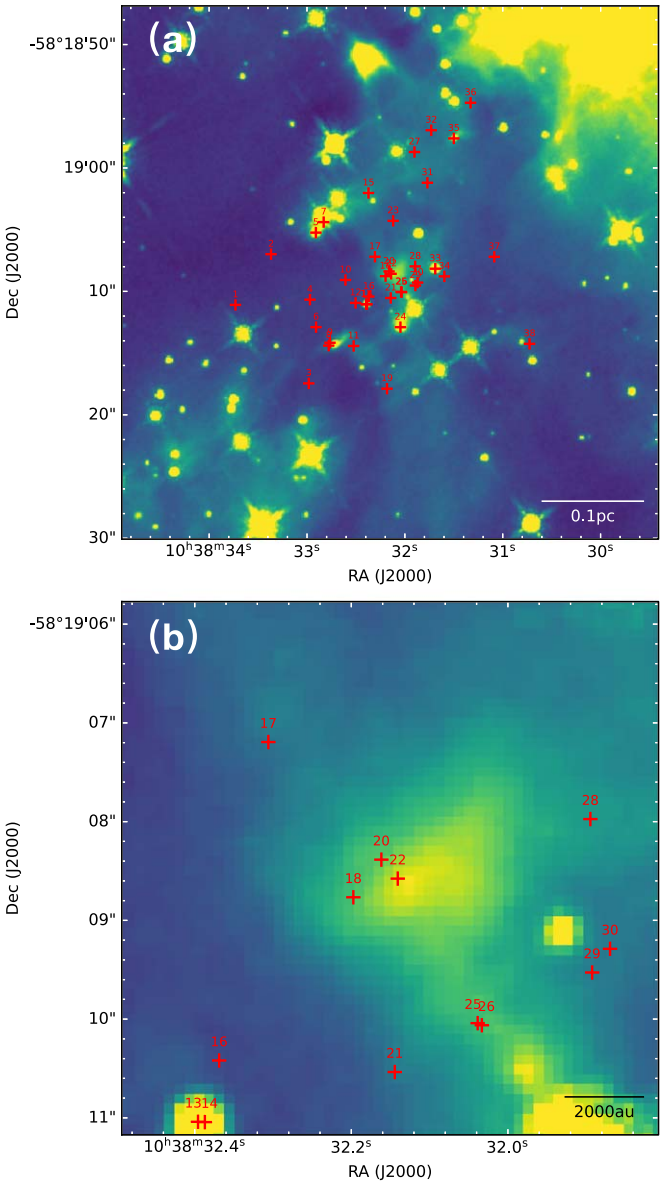

Figure A1. (a) F160W map of G286 observed with HST-WFC3/IR. The positions of disks are indicated with red crosses. (b) A zoom-in view of the central 5.″4 field of view.

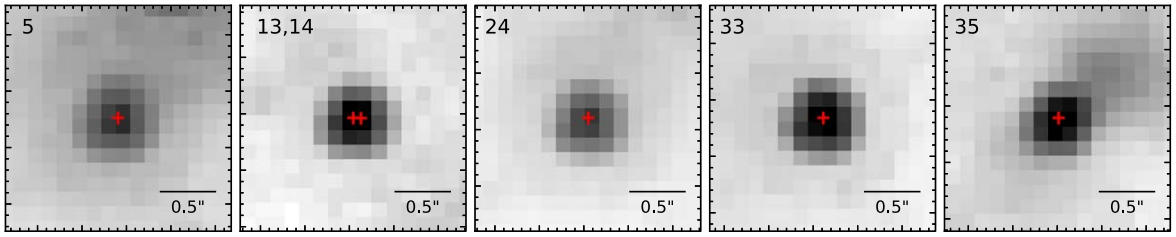

Figure A2. HST F160W image of six disks with NIR counterparts in a zoom-in view (including a close binary system). The index of each source is labeled in the top left corner.

Appendix B
SED Fitting of G286c1

To determine the properties of massive protostar(s) in the center of G286, we searched for infrared counterparts of the dense core G286c1 from near-IR to far-IR bands. We retrieved the data sets in the archive including Spitzer 3.5, 4.5, 5.8, and 8.0 μm, Wide-field Infrared Survey Explorer (WISE) 12 and 22 μm, and Herschel 70, 160, 250, 350, and 500 μm maps. Figure B1 presents a zoom-in view of the infrared images for each core from 3.6 to 350 μm. We use aperture photometry to measure the fluxes in each band, with a fixed aperture radius of 17″. This aperture size is determined using an automated method described in Fedriani et al. (2022), which is based on the gradient of the background-subtracted enclosed flux at 70 μm.

Aperture photometry is carried out following the method of Liu et al. (2019), i.e., we carry out a background subtraction using the median flux density in an annular region extending from one to two aperture radii, to remove general background and foreground contamination. The error bars are set to be the larger of either 10% of the background-subtracted flux density or the value of the estimated background flux density. Note that the flux measurement for $\lambda < 8.0\,\mu$m is most likely overestimated since the adopted aperture also covers emission from surrounding sources. This will not significantly affect our SED fitting results since in our SED modeling the data points of shorter wavelengths (<8.0 μm) are treated as upper limits (see De Buizer et al. 2017, for more details). We also note that we did not use the photometry at 500 μm in the SED fitting because the adopted aperture is smaller than the spatial resolution.

We utilize the Python package *sedcreator* to fit the IR to millimeter SEDs toward G286c1 (Fedriani et al. 2022), which is based on radiative transfer models of Zhang & Tan (2018; ZT models hereafter). The ZT model is a continuum radiative transfer model that describes the evolution of high- and intermediate-mass protostars with analytic and semianalytic solutions based on the paradigm of the turbulent core model (see Zhang & Tan 2018, for more details). The main free parameters in this model are the initial mass of the core M_c, the mass surface density of the clump that the core is embedded in $\Sigma_{\rm cl}$, the protostellar mass m_*, as well as other parameters that characterize the observational setup, i.e., the viewing angle $\theta_{\rm view}$ and the level of foreground extinction A_V.

Figure B2 shows the best-fit SEDs for G286c1, with the parameters for the best five fitted models reported in Table B1. If we consider the typical parameter ranges among the best five models as an initial constraint for the protostellar system, G286c1 can be fitted with a protostellar source with a central mass of 4–12 $M_\odot$, with an accretion rate of (0.9–7.0) $\times$ $10^{-4}\,M_\odot\ {\rm yr}^{-1}$. Such large ranges reflect the model degeneracy that exists in trying to constrain protostellar properties from only their mid-IR to far-IR SEDs (De Buizer et al. 2017), especially given that the fluxes at 10–50 μm are not well constrained in our case. Following Fedriani et al. (2022), we also list the parameters for the average and dispersion of all the "good" models, defined as models that satisfy $\chi^2 < 2$. This

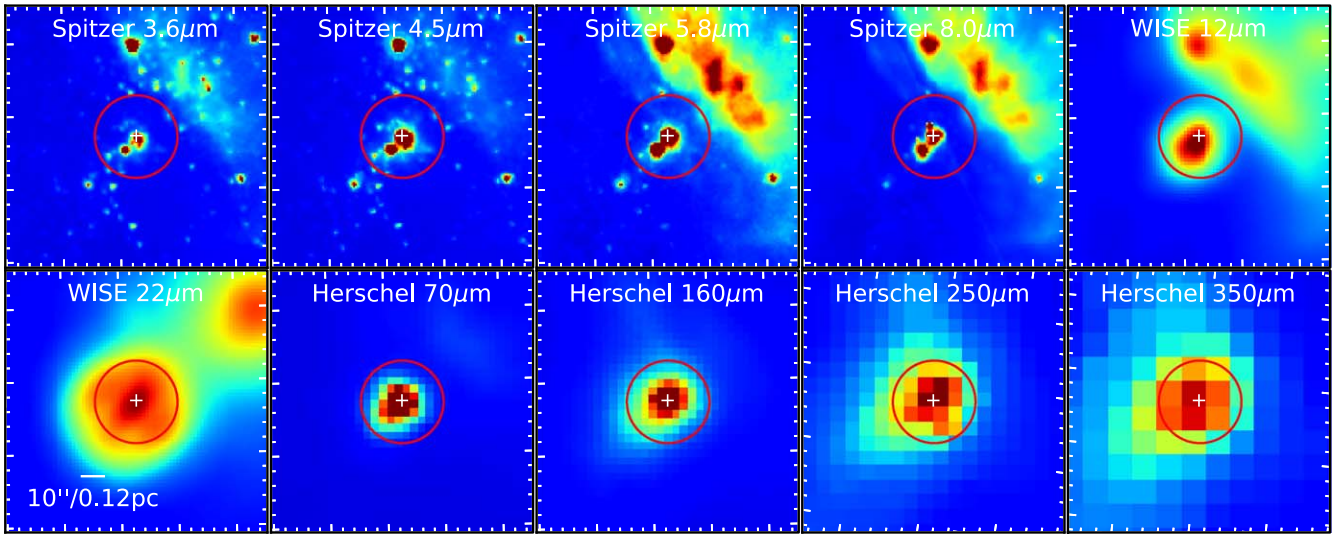

Figure B1. Maps of G286c1 in different wavelengths observed with Spitzer, WISE, and Herschel. The position of G286c1 is marked with a white cross. The red circles indicate the aperture used for photometry.

Table B1
Parameters of the Best Five Fitted Models for G286c1[a,b]

Source	χ^2	M_c ($M_\odot$)	$\Sigma_{\rm cl}$ (g cm^{-2})	m_* ($M_\odot$)	$R_{\rm core}$ (pc)	$\theta_{\rm view}$ (deg)	A_V (mag)	$\theta_{\rm w,esc}$ (deg)	$m_{\rm disk}$ ($M_\odot$)	$r_{\rm disk}$ (au)	$\dot{m}_{\rm disk}$ ($M_\odot$ yr^{-1})	$L_{\rm bol,iso}$ ($L_\odot$)	$L_{\rm bol}$ ($L_\odot$)
G286c1	0.21	80	3.2	4.0	0.04	22	15.7	14	1.3	18	5.1×10^{-4}	0.9×10^4	0.8×10^4
$d = 2.5$ kpc	0.28	80	3.2	8.0	0.04	22	230.8	19	2.7	30	7.0×10^{-4}	1.8×10^4	3.1×10^4
$R_{\rm ap} = 17''$	0.34	240	0.1	12.0	0.36	29	138.6	19	4.0	179	0.9×10^{-4}	2.0×10^4	1.7×10^4
$R_{\rm ap} = 0.21$pc	0.35	160	1.0	8.0	0.09	13	281.1	13	2.7	46	3.6×10^{-4}	1.3×10^4	6.2×10^4
	0.36	480	0.3	8.0	0.29	13	168.3	8	2.7	65	2.0×10^{-4}	0.9×10^4	1.9×10^4
Average model	(#1325)	156^{143}_{75}	$0.4^{1.2}_{0.3}$	$14.0^{16.0}_{7.5}$	$0.14^{0.22}_{0.09}$	56 ± 22	194 ± 149	29 ± 17	$4.7^{5.3}_{2.5}$	116^{187}_{71}	$2.1^{2.6}_{1.2} \times 10^{-4}$	$2.6^{8.1}_{2.0} \times 10^4$	$4.0^{11.6}_{3.0} \times 10^4$

Notes.

[a] The first five rows refer to the best five models taken from the 432 physical models, whereas the sixth row shows the average and dispersion of "good" model fits (see text). Super- and subscripts in the row for average models refer to the upper and lower ends of the dispersion interval.

[b] From left to right, the parameters are reduced χ^2, the initial core mass M_c, the mean mass surface density of the clump $\Sigma_{\rm cl}$, the current protostellar mass m_*, the core radius $R_{\rm core}$, the viewing angle $\theta_{\rm view}$, foreground extinction A_V, half opening angle of the outflow cavity $\theta_{\rm w,esc}$, the mass of the disk $m_{\rm disk}$, the radius of the disk $r_{\rm disk}$, accretion rate from the disk to the protostar $\dot{m}_{\rm disk}$, the luminosity integrated from the unextincted model SEDs assuming isotropic radiation $L_{\rm bol,iso}$, and the inclination-corrected true bolometric luminosity $L_{\rm bol}$. For the average model the second column refers to the number of "good" models.

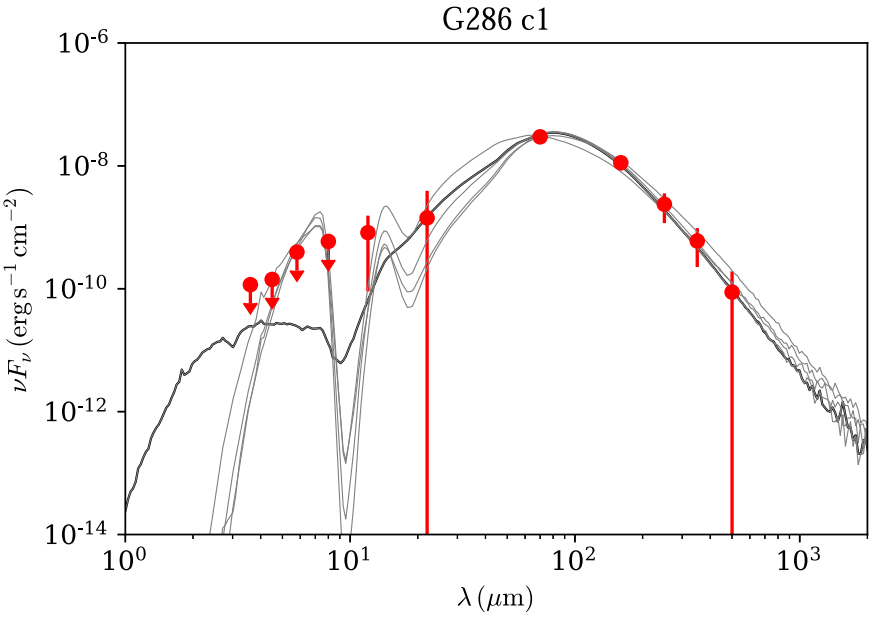

Figure B2. Protostar model fitting to the fixed aperture, background-subtracted SED of G286c1 using the ZT model grid. The best-fit model is shown with a solid black line and the next four best models are shown with solid gray lines.

averaged solution prefers a more massive protostar of $\sim 14.0^{16.0}_{7.5}$ $M_\odot$, embedded in a relatively low-Σ core of $0.4^{1.2}_{0.3}$ g cm^{-2}, and accreting at $2.1^{2.6}_{1.2} \times 10^{-4}\,M_\odot$ yr^{-1}. A caveat in the SED analysis is that we have implicitly assumed the fluxes are mainly contributed by a single protostar, which may not be true for G286c1. G286c1 clearly hosts a triple system and the three components have comparable disk masses.

ORCID iDs

Yu Cheng https://orcid.org/0000-0002-8691-4588
Jonathan C. Tan https://orcid.org/0000-0002-3389-9142
John J. Tobin https://orcid.org/0000-0002-6195-0152
Rubén Fedriani https://orcid.org/0000-0003-4040-4934
Morten Andersen https://orcid.org/0000-0002-5306-4089
Junfeng Wang https://orcid.org/0000-0003-4874-0369

References

Alcock, H. L., & Parker, R. J. 2019, MNRAS, 490, 350
Allison, R. J., Goodwin, S. P., Parker, R. J., et al. 2009, MNRAS, 395, 1449
Andersen, M., Barnes, P. J., Tan, J. C., Kainulainen, J., & de Marchi, G. 2017, ApJ, 850, 12
Ansdell, M., Williams, J. P., Manara, C. F., et al. 2017, AJ, 153, 240
Ansdell, M., Williams, J. P., van der Marel, N., et al. 2016, ApJ, 828, 46
Aravena, M., Decarli, R., Walter, F., et al. 2016, ApJ, 833, 68
Armitage, P. J. 2011, ARA&A, 49, 195
Astropy Collaboration, Robitaille, T. P., Tollerud, E. J., et al. 2013, A&A, 558, A33
Barenfeld, S. A., Carpenter, J. M., Ricci, L., & Isella, A. 2016, ApJ, 827, 142
Barnes, P. J., Yonekura, Y., Ryder, S. D., et al. 2010, MNRAS, 402, 73
Bate, M. R. 2018, MNRAS, 475, 5618
Bohlin, R. C., Savage, B. D., & Drake, J. F. 1978, ApJ, 224, 132
Busquet, G., Girart, J. M., Estalella, R., et al. 2019, A&A, 623, L8
Cheng, Y., Andersen, M., & Tan, J. 2020a, ApJ, 897, 51
Cheng, Y., Tan, J. C., Liu, M., et al. 2018, ApJ, 853, 160
Cheng, Y., Tan, J. C., Liu, M., Lim, W., & Andersen, M. 2020b, ApJ, 894, 87
Cieza, L. A., Ruíz-Rodríguez, D., Hales, A., et al. 2019, MNRAS, 482, 698
Cox, E. G., Harris, R. J., Looney, L. W., et al. 2017, ApJ, 851, 83
Cutri, R. M., Skrutskie, M. F., van Dyk, S., et al. 2003, VizieR On-line Data Catalog: II/246
Davidson-Pilon, C., Kalderstam, J., Zivich, P., et al. 2019, CamDavidsonPilon/lifelines: v0.21.1, Zenodo, doi:10.5281/zenodo.2652543
De Buizer, J. M., Liu, M., Tan, J. C., et al. 2017, ApJ, 843, 33
Dib, S., & Henning, T. 2019, A&A, 629, A135
Eisner, J. A., Arce, H. G., Ballering, N. P., et al. 2018, ApJ, 860, 77
Encalada, F. J., Looney, L. W., Tobin, J. J., et al. 2021, ApJ, 913, 149
Federman, S., Megeath, S. T., Tobin, J. J., et al. 2022, arXiv:2210.07925
Fedriani, R., Tan, J. C., Telkamp, Z., et al. 2022, arXiv:2205.11422
Feigelson, E., Townsley, L., Güdel, M., & Stassun, K. 2007, in Protostars and Planets V, ed. B. Reipurth, D. Jewitt, & K. Keil (Tucson, AZ: Univ. Arizona Press), 313
Feigelson, E. D., & Montmerle, T. 1999, ARA&A, 37, 363
Fujimoto, S., Ouchi, M., Ono, Y., et al. 2016, ApJS, 222, 1
Gennaro, M., Brandner, W., Stolte, A., & Henning, T. 2011, MNRAS, 412, 2469
González-López, J., Novak, M., Decarli, R., et al. 2020, ApJ, 897, 91
Hollenbach, D. J., Yorke, H. W., & Johnstone, D. 2000, in Protostars and Planets IV, ed. V. Mannings, A. P. Boss, & S. S. Russell (Tucson, AZ: Univ. Arizona Press), 401
Kirk, H., Johnstone, D., Di Francesco, J., et al. 2016, ApJ, 821, 98
Li, Z.-Y., Krasnopolsky, R., Shang, H., & Zhao, B. 2014, ApJ, 793, 130
Liu, M., Tan, J. C., De Buizer, J. M., et al. 2019, ApJ, 874, 16
Manara, C. F., Ansdell, M., Rosotti, G. P., et al. 2022, arXiv:2203.09930
Manara, C. F., Tazzari, M., Long, F., et al. 2019, A&A, 628, A95
Mann, R. K., Di Francesco, J., Johnstone, D., et al. 2014, ApJ, 784, 82
McKee, C. F., & Tan, J. C. 2003, ApJ, 585, 850
McMullin, J. P., Waters, B., Schiebel, D., Young, W., & Golap, K. 2007, in ASP Conf. Ser. 376, Astronomical Data Analysis Software and Systems XVI, ed. R. A. Shaw, F. Hill, & D. J. Bell (San Francisco, CA: ASP), 127
Meylan, G. 2000, in ASP Conf. Ser. 211, Massive Stellar Clusters, ed. A. Lançon & C. M. Boily (San Francisco, CA: ASP), 215
Mottram, J. C., Hoare, M. G., Lumsden, S. L., et al. 2007, A&A, 476, 1019
Muñoz Arancibia, A. M., González-López, J., Ibar, E., et al. 2022, arXiv:2203.06195
Nicholson, R. B., Parker, R. J., Church, R. P., et al. 2019, MNRAS, 485, 4893
Nony, T., Robitaille, J. F., Motte, F., et al. 2021, A&A, 645, A94
Ossenkopf, V., & Henning, T. 1994, A&A, 291, 943
Otter, J., Ginsburg, A., Ballering, N. P., et al. 2021, ApJ, 923, 221
Parker, R. J. 2018, MNRAS, 476, 617
Pascucci, I., Testi, L., Herczeg, G. J., et al. 2016, ApJ, 831, 125
Plunkett, A. L., Fernández-López, M., Arce, H. G., et al. 2018, A&A, 615, A9
Robitaille, T., & Bressert, E. 2012, APLpy: Astronomical Plotting Library in Python, Astrophysics Source Code Library, ascl:1208.017
Rosolowsky, E. W., Pineda, J. E., Kauffmann, J., & Goodman, A. A. 2008, ApJ, 679, 1338
Sadaghiani, M., Sánchez-Monge, Á, Schilke, P., et al. 2020, A&A, 635, A2
Sanhueza, P., Contreras, Y., Wu, B., et al. 2019, ApJ, 886, 102
Tobin, J. J., Sheehan, P. D., Megeath, S. T., et al. 2020, ApJ, 890, 130

Tripathi, A., Andrews, S. M., Birnstiel, T., & Wilner, D. J. 2017, ApJ, 845, 44
Tychoniec, Ł., Manara, C. F., Rosotti, G. P., et al. 2020, A&A, 640, A19
van Terwisga, S. E., Hacar, A., van Dishoeck, E. F., Oonk, R., & Portegies Zwart, S. 2022, A&A, 661, A53
Williams, J. P., & Cieza, L. A. 2011, ARA&A, 49, 67
Xu, W. 2022, ApJ, 934, 156
Xu, W., & Kunz, M. W. 2021, MNRAS, 508, 2142
Zhang, Y., & Tan, J. C. 2018, ApJ, 853, 18
Zhang, Y., Tan, J. C., & Hosokawa, T. 2014, ApJ, 788, 166
Zucker, C., Speagle, J. S., Schlafly, E. F., et al. 2020, A&A, 633, A51